

A sticking-erosion model for ice crystal icing at glaciated icing conditions using particle size distribution

Xin Yang*, Matthew McGilvray[†], and David Gillespie[‡]
University of Oxford, Oxford OX2 0ES, UK

Ice crystal icing has been identified as a threat to aviation safety, with hundred engine power loss events having been experienced since the 1990s. This has led to new type certification requirements for the industry to demonstrate safe operation in these environmental conditions. The sticking and erosion behaviours of ice crystals are critical factors in ice crystal icing. However, many existing sticking-erosion models are developed based on ice crystals using the mean particle diameter for experimental tests which have a broad distribution of size. This leads to biasing when a different distribution with the same mean particle diameter is considered. This paper develops a new sticking-erosion model which accounts for the particle size distribution seen in experimental data typical of glaciated icing conditions. The results of model are compared to experimental accretion data over a range of melt ratio, Mach number, test article geometry and particle size distribution. The predicted accretion profiles agree reasonably with experiments. The mean difference of the ice tip thickness between predictions and experiments is approximately 2.8 mm, compared to the mean ice tip thickness of 12.0 mm. The plateau effect of melt ratio on accretion is adequately predicted. More severe accretion of the small-medium sized ice crystals is observed. The predicted net accretion efficiency of large particles ($>D_{v90}$) is small and is shown to be negative due to the effect of erosion. This concurs with the experimental observation that the presence of large ice particles is critical to reducing the ice accretion rate.

I. Nomenclature

D_p	=	particle diameter, m
$D_{v10}, D_{v50}, D_{v90}$	=	maximum diameter of sample containing 10%, 50%, 90% of product by volume
ICI	=	ice crystal icing
L_{ref}	=	reference length, m

*Postdoctoral researcher, Department of Engineering Science, Oxford Thermofluids Institute, AIAA Member; xin.yang@eng.ox.ac.uk (Corresponding author).

[†]Associate Professor, Department of Engineering Science, Oxford Thermofluids Institute.

[‡]Associate Professor, Department of Engineering Science, Oxford Thermofluids Institute.

Ma	=	Mach number
MR	=	Melt Ratio, [-]
MRD	=	mean relative difference, [-]
MVD	=	median volume diameter, m
OAE	=	overall accretion efficiency, [-]
OEE	=	overall erosion efficiency, [-]
OIE	=	overall impingement efficiency, [-]
OSE	=	overall sticking efficiency, [-]
P_e	=	erosion efficiency, [-]
P_s	=	sticking efficiency, [-]
PSD	=	particle size distribution
t	=	time, s
TWC	=	total water content, g/m^3
V_p	=	particle velocity magnitude, m/s
X	=	x-coordinate of the ice shape, m
Y	=	y-coordinate of the ice shape, m
θ	=	impingement angle, $^\circ$
θ_h	=	cone half angle, $^\circ$

II. Introduction

Ice crystal icing (ICI) is recognised as a threat to jet engines. Since 1990, there have been more than 150 jet engine power loss events possibly due to ICI [1–3]. Due to the threat, new certification requirements have been introduced by FAA in Amendment 34 of 14 CFR 33 and by EASA in Amendment 4 of CS-E and Amendment 16 of CS-25. Several ice crystal icing codes have been developed to support the design and certification of engines/aircrafts, including GlennICE from NASA [4], IGLOO2D from ONERA [5, 6], FENSAP-ICE by Habashi et al. [7], MooseMBIce extended by Norde et al. [8, 9], as well as ICICLE at Oxford [10, 11]. Understanding the sticking and erosion behaviours of ice crystals is an important element to develop a mathematical model of the phenomenon to introduce in icing codes.

Early development of sticking-erosion models of ice crystals was undertaken for mixed-phase conditions for temperatures below the freezing point of water. These conditions are relevant to icing at engine inlets of external aircraft components. Lozowski et al. [12] proposed a sticking model for ICI, where ice crystals were assumed to bounce off dry walls and stick to wet walls (or at least, freeze all the existing water on the surface). Nilamdeen et al. [7] presented a proof-of-concept sticking model, which is a function of particle size, velocity and film thickness. The model

assumed ice crystals to partially stick to walls in the glaze icing regime while it adopted an assumption for dry and wet walls similar to Lozowski et al. [12]. Wright et al. [4] developed a model assuming that ice crystals could partially accumulate to wet walls with the sticking efficiency being dependent on a restitution coefficient. Similar to Lozowski et al. [12] and Nilamdeen et al. [7], it is assumed that ice crystals cannot stick to dry walls in the model. Different from the sticking model by Nilamdeen et al. [7], this model proposed an empirical erosion sub-model as a function of particle size, velocity, ice water content and accretion surface temperature. The model constants were derived from icing test data at different median volume diameter (MVD) and water content from the Cox icing wind tunnel [13]. Recently, Ayan et al. [14] modified the constants of the empirical erosion sub-model using test data from the Braunschweig icing wind tunnel [15].

With the increased interest in ICI in engine cores, where warm gas temperatures above freezing point are expected, some new or refined sticking-erosion models have been developed in recent years. The sticking model proposed by Nilamdeen et al. [7] for ICI at mixed-phase conditions was adapted through the addition of a dependency on particle melt ratio (MR) allowing partially melted particles to stick to walls [16]. The modified model adequately predicted an ice accretion on a crowned cylinder test article. Currie et al. [17] proposed an empirical sticking model for predicting ICI based on measurements in the RATFac icing wind tunnel. The model is limited to the optimum melt ratio range (approximately 10-23% by Currie et al. [17] and 9-13% by Bucknell et al. [18]), where the peak ice accretion rate was observed. Particle net sticking behaviour was assumed to be dependent on total water content (TWC), surface normal angle and particle velocity. The term of TWC, having a value in the range of 0.86 to 1, was used to consider the flux effect, which could decrease the erosion rate at high TWC. The model adequately predicted the accretion profile at different TWCs on three test articles (including crowned cylindrical/spherical/conical test articles) although the accretion thermodynamics was not considered in the model. Recently, Currie et al. [19] modified the sticking model by adding a term of particle size in order to consider its effect on erosion.

Unlike previous sticking models cited above, Trontin et al. [20] attempted to isolate the contributions of sticking and erosion behaviour on ICI and presented an empirical sticking-erosion model. Particle sticking efficiency was assumed to increase from zero to unity with increasing MR from zero to unity. The empirical correlation was derived based on the ice growth rate near the stagnation point again using test data from a RATFac test article. Here, the erosion model was assumed to be a function of particle tangential impingement velocity, wall liquid mass fraction and surface curvature. The sticking-erosion model adequately predicted the accretion profiles below the optimum MR range while obviously over-predicting the ice accretion rate above the optimum MR range. Charton et al. [21] developed a semi-empirical erosion model based on solid-solid collision theory considering both deformation and cutting erosion. Young's modulus and compressive yield strength of the icing layer were assumed to be linearly dependent on the MR of the ice layer. An effective particle velocity was evaluated using the dynamic fracture theory for brittle materials in order to obtain an explicit dependency of the erosion rate on particle size. The model attempted to predict a lower ice accretion rate above

the optimum MR range at $Ma = 0.25$ than that using the erosion model by Trontin et al. [20]. The model predicted the experimentally observed conical accretion shape at $Ma = 0.48$ and $MVD = 28 \mu m$. However, the semi-empirical model over-predicted the accretion rate at the conditions below the optimum MR range for the crowned cylinder test article at $Ma = 0.25$. The model obviously over-predicted the ice accretion rate above the optimum MR range at $Ma = 0.4$. Recently, Bucknell et al. [18] developed an empirical sticking-erosion model, which managed to split the contributions of sticking and erosion behaviours on ICI. Unlike the sticking model by Trontin et al. [20], particle sticking efficiency was assumed to gradually increase from 0 to unity over the range of MR from 0 to the optimum MR = 0.13 and then decrease from unity to 0 with further increases of MR up to MR=0.34. The efficiency was set as 0 for $MR > 0.34$. This assumption was used to improve the prediction performance of the accretion profile for MR greater than the optimum range, however, it may also under-predict the contribution of small-medium particles on sticking. In this model, the particle erosion model was assumed to be a function of a quasi-kinetic energy parameter, surface normal angle and accretion surface temperature. The predicted ice removal efficiency using the sticking-erosion model matched the experimental data well.

Table 1 Ice crystal sticking-erosion models reported in literature.

Condition	Reference	Sticking-erosion model
Mixed-phase	Lozowski et al. 1983 [12]	Bounce off dry walls; Stick to wet walls.
	Nilamdeen et al. 2011 [7]	Partially stick to walls in the glaze icing regime; sticking efficiency is a function of particle size, velocity and film thickness; Mean particle size is used.
	Wright et al. 2010 [4]	Sticking efficiency is a function of restitution coefficient; Erosion efficiency is a function of particle size, velocity, ice water content and accretion surface temperature; Mean particle size is used.
Glaciated	Nilamdeen et al. 2019 [16]	Modified from their model [7] by adding the term of particle melt ratio; Mean particle size is used.
	Currie et al. 2014 and 2019 [17, 19]	Net sticking efficiency is a function of particle melt ratio, total water content, surface normal angle, particle velocity and particle size.
	Trontin et al. 2018 [5]	Sticking efficiency is a function of particle melt ratio; Erosion efficiency is a function of particle tangential impingement velocity, wall liquid mass fraction and surface curvature; Mean particle size is used.
	Charton et al. 2020 [21]	Sticking efficiency is a function of particle melt ratio; Erosion efficiency is calculated using a semi-empirical model based on the solid-solid collision theory; Mean particle size is used.
	Bucknell et al. 2020 [18]	Sticking efficiency is a function of particle melt ratio; Erosion efficiency is a function of particle kinetic energy, surface normal angle, accretion surface temperature; Mean particle size is used.

Overall, these sticking-erosion models (as shown in Table 1) have made significant progress in modelling ICI and understanding icing physics. However, many of these existing models were developed based on mean particle

size in order to simplify the necessity of having to deal with a large number of particle impingement data when the particle size distribution (PSD) is considered. This may lead to inaccuracies when modelling ICI with the different particle size distributions. Existing ICI tests in the RATFac icing wind tunnel have already confirmed that the PSD is significant in determining ice accretion, especially for the largest particles ($Dv90$) [18, 22]. The present study aims 1) to develop a sticking-erosion model at individual particle-scale and 2) to improve the understanding in the contribution of particle size on ICI. Modelling ICI is carried out using the in-house icing code, ICICLE [10]. Development of the new sticking-erosion model is based on the individual particle impingement behaviour (particle MR, velocity, impingement angle and size) predicted by ICICLE and experimental accretion data, which covers operation conditions at varied MR, Ma, test article and PSD. Results of simulations using this new model are compared to experimental data to show its performance.

III. Mathematical models

This section describes the underlying basis and requirements for each part of the mathematical models of the physics employed in the current study.

A. Sticking-erosion model

The mass flux of ice crystal accretion is determined by the deposited flux of impinging ice particles and the thermodynamic accretion model taking into account the erosion effect. Therefore, a sticking-erosion model is required to (i) predict the sticking efficiency of impinging ice particles, which is defined by the mass fraction of the impinging ice-particle mass flux that will stick on walls and (ii) predict the erosion efficiency, which is defined by the ratio of the dislodged accretion mass flux to the impinging mass flux.

1. Sticking

The sticking behaviour of ice particles is dictated by particle physical properties (including melt ratio, particle size, velocity, impingement angle, particle shape, etc.) and accretion surface properties (e.g. wet surface, dry surface, heated surface.). It is challenging to develop an analytical sticking model for ICI due to the complexity of the phenomenon itself and the difficulty in experimentally decoupling the effects of these physical properties on ICI. Therefore, an empirical sticking model is proposed according to the following assumptions.

- The sticking efficiency is assumed to only depend on melt ratio and the direct effects of particle velocity and size on particle sticking efficiency are neglected. This assumption is similar to that used in previous sticking models proposed by Trontin et al. [20] and Bucknell et al. [18]. Although the effect of particle size is not considered, it is expected that the sticking efficiency will still increase with the decrease in particle size since smaller ice particles are easier to melt.

- Both particle melt ratio and the liquid mass fraction of the accretion surface (referred to as accretion melt ratio) can contribute to particle sticking. Therefore, it is assumed that the sticking efficiency is dependent on both particle melt ratio and accretion melt ratio, represented by Equation (1). This assumption is commonly used for predicting particle sticking efficiency in the field of particle deposition studies [23, 24].
- The accretion melt ratio is assumed to be represented by the mass-averaged melt ratio of the impinging ice particles on a local wall surface. This reduces the dependency of the sticking model on the thermodynamic accretion model. This assumption may be justified by the experimental observation by Currie et al. [25] and Trontin et al. [20], where the measured particle mean melt ratio, ranged from approximately 6% to 40% is correlated to the experimentally derived accretion melt ratio, ranged from approximately 6% to 45%.
- The expression of sticking efficiency as a function of melt ratio proposed by Trontin et al. [20], represented by Equations (2) and (3). The expression is developed based on the experimental ice crystal icing behaviour at the stagnation point of a crowned cylinder, is implemented in this study in order to reduce the complexity to develop a new sticking-erosion model. In the expression, the sticking efficiency will gradually increase from zero to unity with increasing melt ratio from zero to unity. This is in accordance with the conditions that a fully solid ice particle will mostly bounce off dry walls and a fully liquid ice particle will mostly stick to walls or an ice particle will stick to wet walls.

Therefore, based on the above assumptions, the sticking efficiency of an impinging ice particle, P_s , is predicted based on individual particle melt ratio, MR_p , and local mean impingement particle melt ratio on a wall surface, MR_m :

$$P_s = P_{s,p} + (1 - P_{s,p})P_{s,s} \quad (1)$$

$$P_{s,p} = 0.5MR_p^3 - 2.0MR_p^2 + 2.5MR_p \quad (2)$$

$$P_{s,s} = 0.5MR_m^3 - 2.0MR_m^2 + 2.5MR_m \quad (3)$$

where, P_s is particle sticking efficiency, $P_{s,p}$ and $P_{s,s}$ are particle sticking efficiencies contributed by individual particle melt ratio and mean impingement particle melt ratio, respectively; MR_p and MR_m are individual particle melt ratio and mean impingement particle melt ratio, respectively.

2. Erosion

A portion of ice accretion could be dislodged by the impinging ice particles. According to the solid-solid collision theory proposed by Finnie et al. [26] and Bitter [27, 28], if particle impingement velocity is above the critical particle elastic velocity, deformation wear and cutting wear will occur. The erosion behaviour is dictated by particle impingement velocity, angle and surface properties, as well as particle size. Considering the fact that the effect of particle velocity and size on ICI are not considered in the sticking model, but only considered in the erosion model, an empirical erosion

model is proposed to predict the erosion efficiency as a function of these parameters based on the following assumptions.

- Increasing particle velocity can reduce the ice accretion rate. This phenomenon has been observed by the ICI tests conducted by Currie et al. [17] and Bucknell et al. [18]. Therefore, it is assumed that the erosion efficiency increases with the increase in particle impingement velocity magnitude. Many of the existing erosion models reviewed earlier in this paper assume that the erosion efficiency is dependent on the particle velocity squared, V_p^2 . Recently, Kott et al. [29] observed that the erosion rate of solid ice crystals approximately doubled by increasing Mach number from 0.4 to 0.5 and three times by increasing Ma from approximately 0.4 to 0.6. This observation is roughly comparable to the dependence on V_p^2 . Therefore, in this study, the same dependence on V_p^2 is implemented in the empirical erosion model, represented by the term ① in Equation (4).
- Increasing particle size, D_p , can efficiently reduce the ice accretion rate based on the experimental observations by Knezevici et al. [22] and Bucknell et al. [18]. This is because increasing particle size will reduce the melting potential and increase particle kinetic energy. Correspondingly, larger particles should have higher erosion efficiency, as well as lower sticking efficiency. Therefore, it is assumed that erosion efficiency will increase with the increase in particle size, represented by the term ② in Equation (4).
- Existing ICI tests have shown that the ice accretion rate reduces with increasing particle MR above the optimum MR [17, 18]. This indicates that it is easier to erode and wash an ice layer off walls if it has a higher accretion melt ratio. Therefore, it is assumed that erosion efficiency is dependent on accretion melt ratio. Similar to the assumption in the sticking model, particle mean melt ratio is used to represent the accretion melt ratio. The term ③ in Equation (4) is used to capture the experimentally observed erosion behaviour as a function of the mean MR.
- The expression for the erosion efficiency is assumed to be a function of the impingement angle, θ , represented by the term ④ in Equation (4). This is in accordance with that proposed by Neilson et al. [30]. In the expression, both cutting wear and deformation wear are taken into account using the cos and sin terms, respectively.

According to the above assumptions, the erosion efficiency of an impinging ice particle, P_e , is predicted by:

$$P_e = A \underbrace{\left(\frac{V_p}{V_{ref}}\right)^2}_{①} \underbrace{\left(\frac{D_p}{D_{ref}}\right)^B}_{②} \underbrace{\left(\frac{C + D \times MR_m}{E + F \times MR_m + G \times MR_m^2 + H \times MR_m^3 + MR_m^4}\right)}_{③} \underbrace{\left(I(\cos \theta)^J + K(\sin \theta)^L\right)}_{④} \quad (4)$$

where, V_{ref} and D_{ref} are the reference velocity and diameter = 1 m/s and $1\mu m$ respectively, used to maintain non-dimensionality; the symbols from **A** to **L** are the model constants, which are derived by an optimization method using the experimentally derived overall erosion efficiency as training data. The training data cover 4 sets of baseline test data with different melt ratios and 3 sets of test data with different Ma/particle size distribution/cone half angle, as shown in VI.A. Figure 1 shows a schematic diagram of the optimization process used in this study. The optimization process is accomplished by combining experimental ice accretion data processing, ICICLE particle tracking and ICICLE

overall erosion efficiency prediction using a constrained nonlinear multi-variable minimisation algorithm to find the optimal values of model constants. Particle tracking is carried out to obtain the particle impingement behaviour (particle velocity, particle size, melt ratio, and impingement angle), which covers all the individual particle data in the particle size distribution. The experimental overall erosion efficiency is derived by (i) the experimental net growth rate processed from icing videos and (ii) the predicted particle sticking efficiency by the particle tracking data and the proposed sticking model. The fmincon algorithm in Matlab is used to find the optimal 12 model constants (A to L) using individual particle impingement data and the sum of the absolute difference of the experimental and predicted overall erosion efficiency is implemented as the objective function. Figure 2 shows the absolute value of the difference of the predicted overall erosion efficiency and data from experiments and Table (2) shows the optimized model constants*.

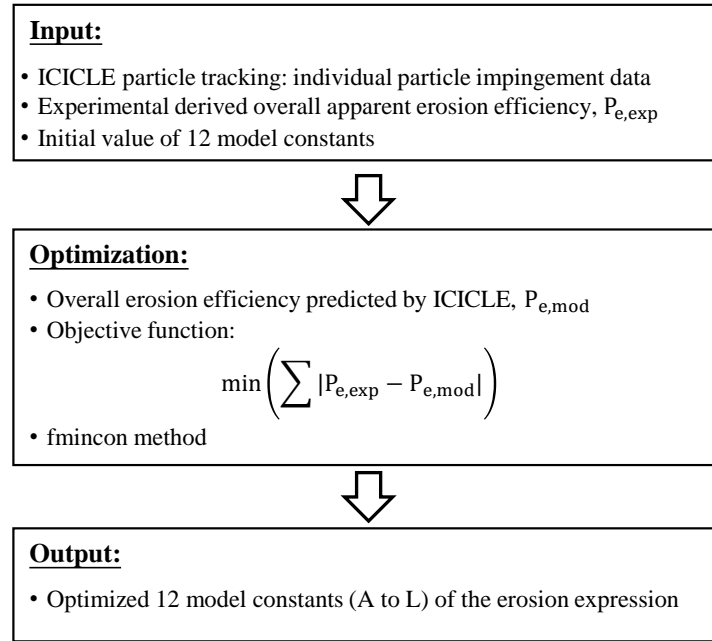


Fig. 1 Schematic diagram of the optimization method to find the model constants for the erosion expression.

Table 2 The optimized model constants (A to L) for the erosion model, Equation(4).

A	B	C	D	E	F
6.30×10^{-5}	9.78×10^{-1}	2.72×10^{-7}	4.37×10^{-5}	1.76×10^{-3}	-3.37×10^{-2}
G	H	I	J	K	L
3.06×10^{-1}	-9.74×10^{-1}	9.20×10^{-1}	2.48	8.00×10^{-1}	2.49

*The optimized model constants for the term ③ (C to H) are valid for $MR_m < 0.41$. For MR_m above 0.41, it may assume that no ice accretion will form according to the ICI tests carried out at the RATFac icing wind tunnel by Bucknell et al. [18].

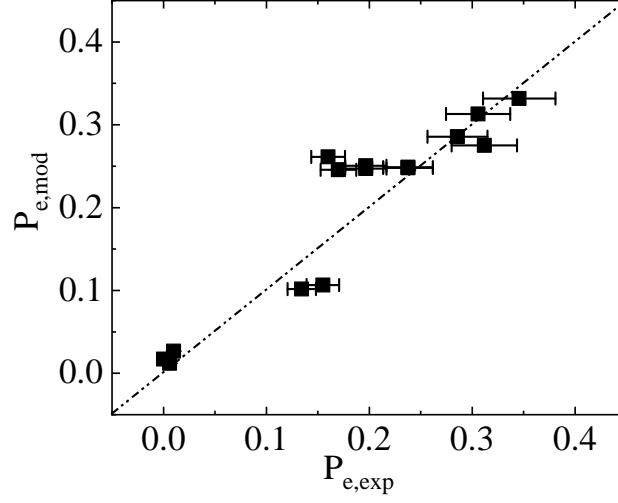


Fig. 2 Comparison of the predicted overall erosion efficiency, $P_{e,mod}$ using the optimized 12 model constants against experiments.

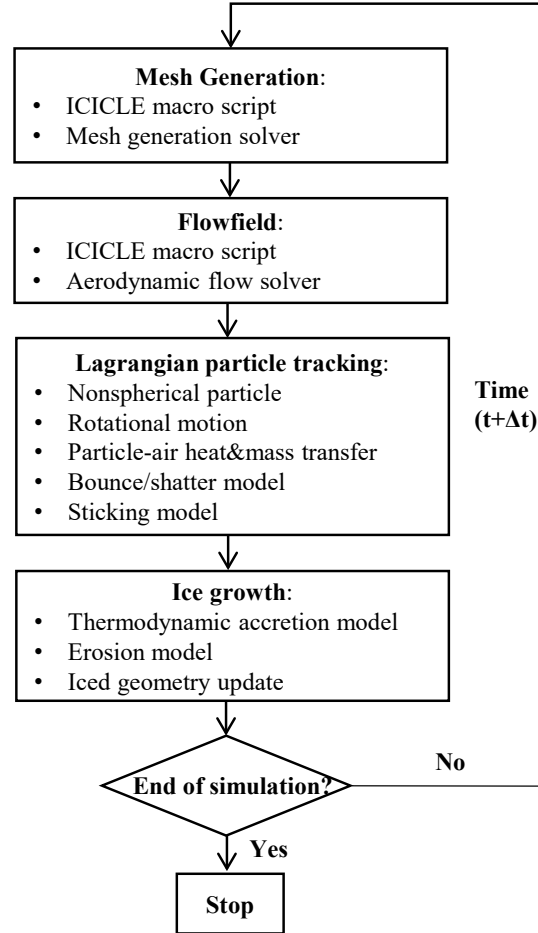


Fig. 3 The algorithm of ice crystal icing modelling in Oxford in-house icing code, ICICLE.

B. ICI modelling

The Oxford in-house icing code, ICICLE, has been used to develop the sticking-erosion model and predict ICI. As shown in Fig. 3, ICICLE has four main components, including mesh generation, flowfield, Lagrangian particle tracking and ice growth as described below. (1) An external mesh generation solver (i.e. Ansys ICEM-CFD) is called by ICICLE to automatically create mesh. In this study, structured meshes are employed due to their advantages in speed of convergence and memory cost. For a test body where ice has accumulated, the geometry is smoothed using an approach which conserves the ice mass [31] before a new mesh is created. (2) The flowfield is calculated by the resolution of the steady-flow Reynolds-averaged Navier–Stokes equations (RANS) using the external aerodynamic flow solver, ANSYS Fluent 19.2. The realizable $k-\epsilon$ turbulence model with scalable wall functions is used to simulate the turbulence. (3) A Lagrangian particle tracking solver is coded in ICICLE to calculate particle trajectories by solving the non-spherical particle translational and rotational motion equations [11]. The melting behaviour of ice crystals, which contains the information of particle melt ratio, is calculated by its particle-air heat & mass transfer model [32]. The outcome of particle impingement on walls is determined by its particle wall interaction model, where particle bounce and shatter behaviours are calculated using the method proposed by Villedieu et al. [5] and the rebound angular velocity is predicted using the method by Tsuji et al. [33]. The particle sticking model is implemented in the Lagrangian particle tracking solver. (4) An ice growth solver is built in ICICLE to calculate ice accretion rate and update the iced geometry. Ice accretion rate is predicted by a three-layer thermodynamic model adapted from the extended Messinger model for ICI [34]. The new particle erosion model is developed in the ice growth solver for calculating net ice accretion rate. More details of the particle tracking solver and ice growth solver can be found in [10, 11, 32, 34].

IV. Case description and setup

A. Case description

ICI experiments used to populate and validate the models developed were conducted in the Research Altitude Test Facility (RATFac) at the National Research Council of Canada (NRC / CNRC) [18]. The purpose of the ICI experiments was to improve the understanding of ICI physics and provide a database for the development and validation of ICI methods. The facility consists of an altitude chamber divided into cold and warm sections, as shown in Fig. 4. Ice particles are generated in the cold section using a grinder system. The particles are fed into the warm section of the test rig and mixed with the temperature controlled warm flow of known relative humidity. The mixture travels into the test section cascade (of cross section, 254×132 mm), where the test article is placed. The test article with a total length of 326 mm consisted of a replaceable cone-noses of known half-angle, θ_h , i.e. 35° , and a cylindrical afterbody 110 mm in length. The total water content, liquid water content, relative humidity are measured by an iso-kinetic probe, a multi-wire probe, a TAT-RH probe, respectively. The total temperature and total pressure are measured by a

Kiel probe. Particle size distribution (PSD) was measured using a laser shadowgraphy technique developed by NRC. Discussion about the difference between the PSD of ice crystal particles and the Langmuir distributions for supercooled water droplets is given in Appendix VI.B. Experimental particle melt ratio: the ratio of liquid water to total water content was measured including a correction for the known false particle collection efficiency and response of the multiwire probe employed. Ice accretion was measured using high-definition video recordings of the backlit test article. Two video cameras (5.0 megapixel Avigilon 5.0 MP-HD-DN, 2592×1944 resolution, 12 fps) were placed above the top and starboard windows, providing top and side views. The top view, which was free of ice buildup, was used for post-processing in order to obtain ice growth data. The operation conditions of the experiments can be found in VI.A. Further details on the experiments, facility and instrumentation may be found in [18, 35, 36].

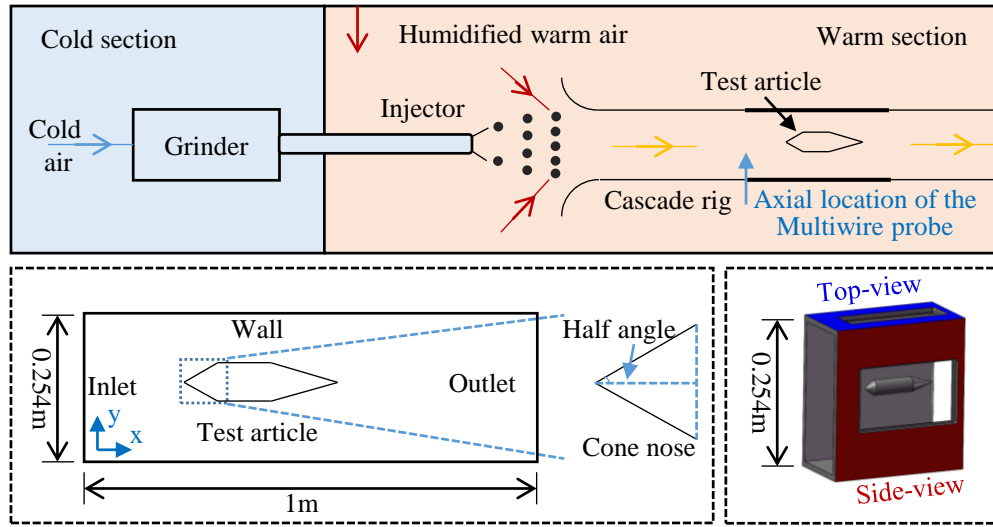


Fig. 4 Schematic diagram of the RATFac icing wind tunnel (on the top), the computational domain of ICI modelling (on the bottom left), and the definition of top view and side view (on the bottom right): not to scale.

B. Numerical case setup

The ICI numerical simulation in this study focuses on the flow region in a reduced flow domain around the test article in order to reduce the computational cost. As shown in Fig. 4, the computational domain is a 2D geometry with the inlet placed at the axial location of the multiwire probe. More details of the discussion about the 2D assumption are given in Appendix VI.D. The boundary conditions (including the inlet pressure, Mach number, TWC and RH) use the values presented in Table (3) of Appendix VI.A. Figure 5 shows the gas temperature at the inlet of the computational domain, which increases from the centre of the flow domain to the outer region. This is because there is a mixing region of the cold air (in the center) for particle injection and hot air of tunnel at the upstream before gases enter the cascade. Particles are injected at the inlet with velocities equal to those of the flow. Particle size at the inlet is characterised by the Rosin-Rammler distribution with 26 bins transferred from the measured particle size distribution from the shadowgraphy

technique. More details of the PSD are given in Appendix VI.B. Particle shape is assumed to be prolate with aspect ratio of 1.5 according to the measured mean particle aspect ratio. The particle initial temperature at the inlet is set to be the freezing point of water as the ice particles are partially melted. The particle initial melt ratio at the inlet is obtained from the in-house simulation of particle melting in the icing wind tunnel with the upstream mixing region. The predicted melt ratio is scaled by the ratio of the measured melt ratio to the mean predicted melt ratio. Figure 6 shows the particle melt ratio used for the baseline case, Test No. 3 (Table (3) of Appendix VI.A), with $Ma = 0.4$, $RH = 0.45$, $Dv50 = 29.5 \mu m$. It is seen that (i) particle melt ratio gradually increases from the centre of working section to the outer region. This is consistent with the gas temperature distribution. It is also observed that particle melt ratio gradually decreases with particle size. Icing time modelled is 120 seconds for all cases of cone test article as shedding occurred after this time for several icing cases. More details of the particle melt ratio used for other cases are given in Appendix VI.E.

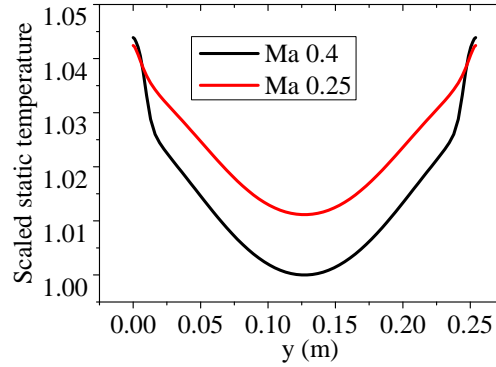


Fig. 5 The static temperature distribution at the inlet of the computational domain used for solving flowfield (the scale ratio is approximately 277.7 K).

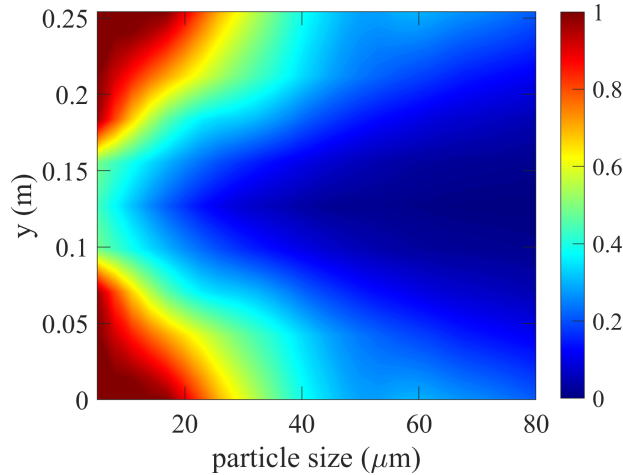


Fig. 6 Particle melt ratio at the inlet of the computational domain vs particle size, baseline case (No.3)

To optimise the computational time required to achieve an accurate solution, a numerical sensitivity study is carried out considering the required resolution of mesh and the number of time sub-steps, N_t . The ice accretion shape, which

can directly represent the severity of ice accretion, is chosen to be the criterion in the numerical sensitivity study [37]. The change in the ice accretion shape is defined as the mean relative difference (MRD) of the accretion height:

$$\text{MRD} = \left(\sum_{i=1}^n \frac{|X_{i,X} - X_{i,Y}|}{L_{\text{ref}}} \right) / n \quad (5)$$

where, $X_{i,X}$ is the x -coordinate of the ice shape (of mesh or the number of time sub-steps), $X_{i,Y}$ is the x -coordinate of the ice shape at the most refined setting (of either the mesh size or the number of time sub-steps); L_{ref} is the reference length representing the distance from the tip of the iced accretion shape at the finest setting to the tip of the clean geometry and is fixed as $L_{\text{ref}} = 0.026$ m; n is the number of grid points on the cone nose. The sensitivity study is carried out using the baseline case (No.3). Figure 7(a) shows the predicted accretion profiles using three different meshes, including a coarse mesh with approximately 12.7 thousand cells, a medium density mesh with approximately 25.6 thousand cells and a fine mesh with approximately 51.7 thousand cells. The MRD is decreased from 12.4% to 2.3% using the medium mesh in replace of the coarse mesh. Hence, the medium refinement mesh, which yields an accretion profile close to that of the fine mesh, is used subsequently. Figure 7(b) shows the predicted accretion profile using three different numbers of the time sub-steps. 20 time sub-steps are chosen for subsequent simulations as the difference in the accretion profile is close to that using 40 sub-steps. The MRD is decreased from 13.4% to 4.4% by increasing the number of sub-steps from 10 to 20. Example meshes of the ice accreted test article generated using the medium density mesh and 20 time sub-steps are shown in Fig. 8. All the CFD solutions are converged although the grid skewness near the cone tip region may increase due to the iced cone tip being sharper than the clean cone tip.

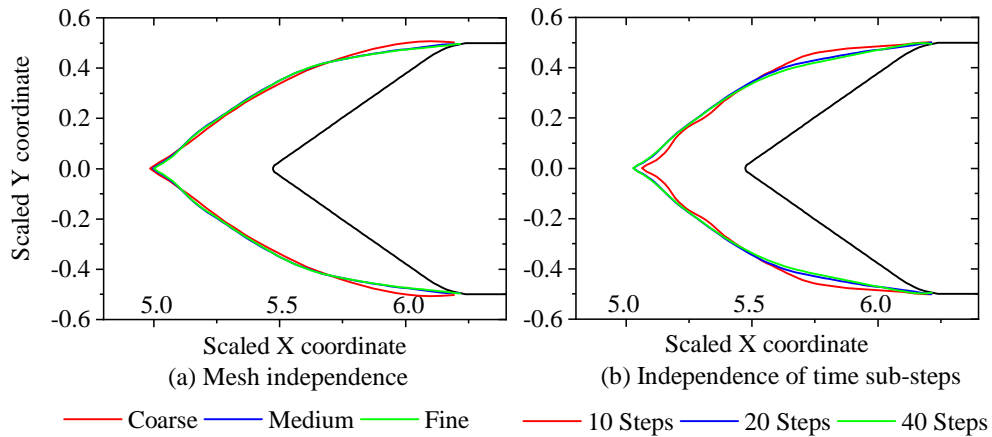


Fig. 7 Mesh and time sub-steps independence study for the baseline case (No.3): (a) mesh independence and (b) independence of time sub-steps.

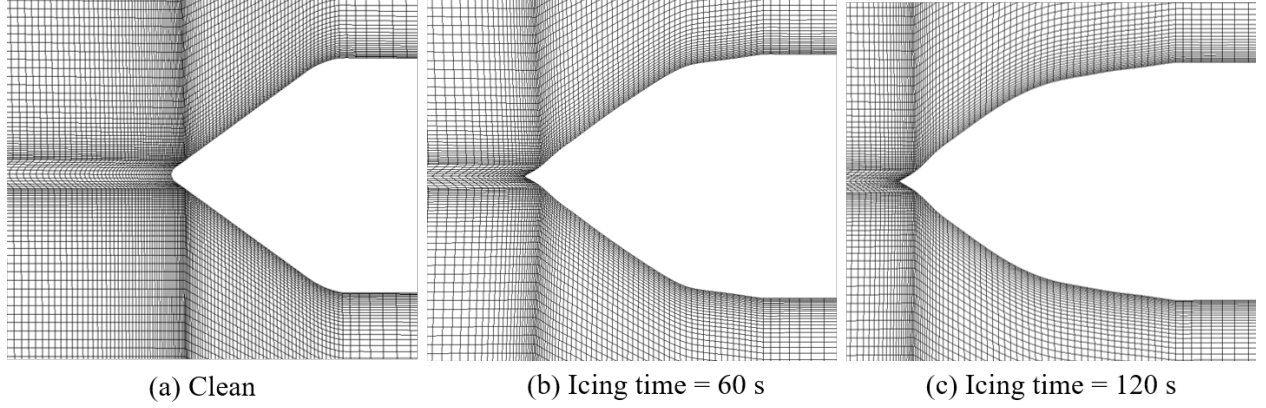


Fig. 8 Examples of the progression of the generated mesh using the medium density mesh and 20 time sub-steps for the baseline case (No. 3) near the cone nose: (a) Clean cone, (b) time = 60 s and (c) time = 120 s.

V. Results and discussions

A. Baseline case (Test No.3)

1. Overall impingement, sticking, erosion and accretion efficiency

The prediction of particle impingement, sticking and erosion behaviours is critical for accurately modelling ICI. Figure 9 shows the Overall Particle Impingement Efficiency (OIE), defined as the ratio of the projected particle impingement mass flux to freestream ice flux; the Overall Sticking Efficiency (OSE), defined as the ratio of the particle sticking mass flux to the particle impingement mass flux; the Overall Erosion Efficiency (OEE), defined as the ratio of the particle erosion mass flux to the particle impingement mass flux; and Overall Accretion Efficiency (OAE), defined as $(OSE - OEE) \times OIE$, which directly represents the ability of ice particles to form ice accretion. These are plotted vs particle size at icing times of 0, 60 and 120 s, resulted from the particle size based overall particle behaviours on the cone nose[†]. In subplot(a) with increasing particle size from 5 to 25 μm , the OIE first sharply increases from approximately 0.2 to 0.75. The OIE then further increases to approximately 0.8 with further increasing particle size to the maximum injected particle size of 80 μm . As smaller particles are less ballistic this decreases their impingement efficiency and makes them more flow following. With increasing icing time, there is a reduction of OIE, on average by approximately 3% and 7% (relative to 0 s) at 60 and 120 s, respectively. The change is more obvious for smaller particles <30 μm , where OIE drops by approximately 5% and 11% (relative to 0 s) at 60 and 120 s, respectively. This is not surprising as smaller particles are more likely to be turned by changes in flow field near the iced surface. In (b) the OSE is seen to decrease from approximately 1 to 0.4 with increasing particle size from 5 to 80 μm . This is because smaller particles are easier to melt and this can increase their sticking efficiency. There is a slight decrease in OSE with time, by approximately 1% and 3% at 60 and 120 s, respectively. This may be because the particle residence time

[†]The particle size used in Fig.9 is taken from each particle size in the Rosin-Rammler based PSD.

reduces with increasing the icing time as the distance travelled by the ice particles is reduced before impingement on the iced surface. In (c), OEE increases from approximately 0 to 0.5 with increasing particle size from 5 to 80 μm . The effect of the icing time on OEE is numerically marginal in this study although the time may affect the local particle erosion efficiency on the iced surface.

As shown in Fig. 9(d), interestingly, OAE first increases from approximately 0.2 to 0.4 with increasing particle size from 5 to 15 μm and then gradually decreases to -0.1 (negative) at particle size of 80 μm . This indicates that there is a selective ice accretion behaviour with a peak accretion efficiency located in the small-medium particle size range for the case investigated. For particle size larger than 65 μm ($>D_{v90}=52 \mu\text{m}$), the accretion efficiency becomes negative. This means the coarse particles rather than contributing to increasing ice accretion, create a net reduction in accreted ice. This is consistent with the previous experimental observations by Knezevic et al. [22] and Bucknell et al. [18] that ICI is particularly sensitive to particle size distribution, especially the largest particle sizes in a distribution represented by D_{v90} . This highlights the importance of considering the full particle size distribution in predicting ICI rather than mean particle size alone. Increasing icing time decreases the OAE. This indicates that the ice accretion rate reduces with time. The average decrease in OAE is approximately 6% and 12% at 60 and 120s.

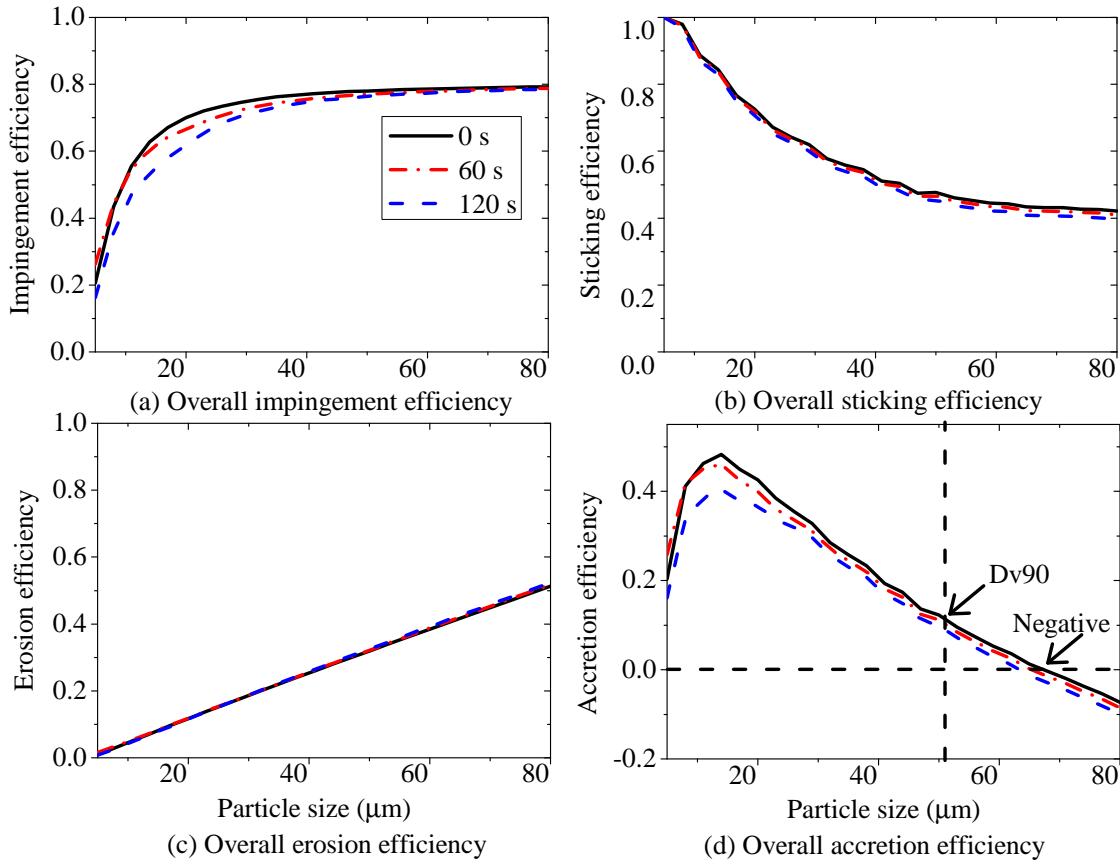


Fig. 9 Particle behaviours as a function of particle size for icing time of 0, 60 and 120 s: (a) overall impingement efficiency, (b) overall sticking efficiency, (c) overall erosion efficiency and (d) overall accretion efficiency.

2. Ice accretion

Figure 10 shows a comparison of the predicted accretion profiles and ice tip thickness against the experimental measurements. It is seen that the predicted accretion profiles and tip thickness quantitatively match well with the experimental results, although the tip thickness is under-predicted by 14% at $t=120$ s. The underprediction of tip thickness may be a result of the performance of the sticking-erosion model. Up to date, it is challenging to fully match the measured icing profiles under multiple operation conditions. The other obvious discrepancy is at the radial outermost location of the cone (highlighted by the green rectangular box in the figure), where in experiment no ice accretion occurs on the cone surface but a low ice accretion is predicted. This region is in close proximity to the large change in surface angle associated with transition from a conical cross-section to a cylindrical cross-section, and ice is able to experimentally shed or to be washed off in this region, as shown in Appendix VI.F. This phenomenon is not taken into account in the current model, and highlights the need for its further development in future work.

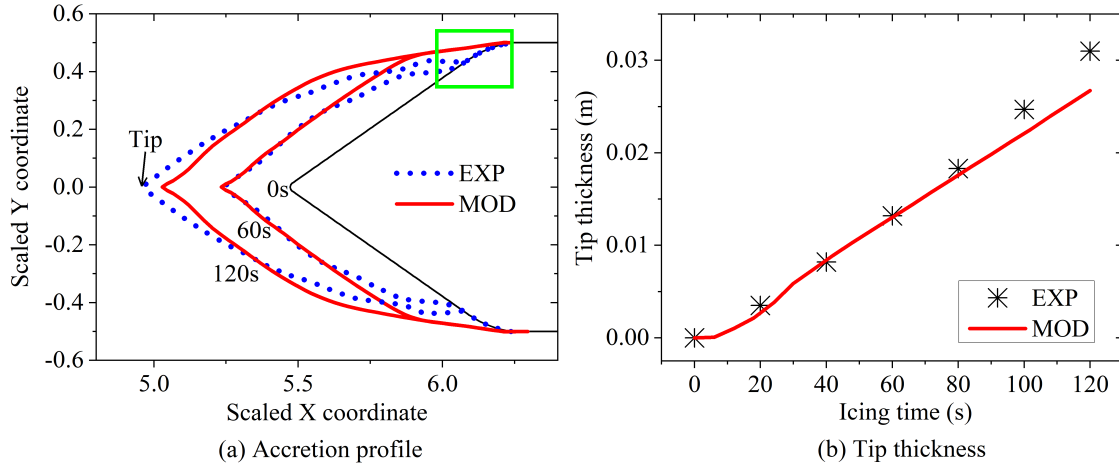


Fig. 10 Comparison of ice accretion predicted (MOD) to the baseline case *vs* experiments (EXP) (a) accretion profile (the scale factor is approximately 0.06m) and (b) tip thickness $Y=0$.

B. The effect of operating conditions on accretion

Figure 11 shows the effect of MR on the accretion profile for $Ma = 0.4$ and $Dv50 = 29.5 \mu m$. The ice accretion rate first increases with MR but then reduces with further increases in MR. This leads to a plateau in the ice accretion rate with increasing MR[‡]. This is because: (i) the particle sticking efficiency increases with particle melt ratio, which increases ice accretion rate; (ii) the particle erosion efficiency increases with the accretion melt ratio, which decreases ice accretion rate. The predicted accretion profiles match well with the experimental profiles at time of $t = 60$ and $t = 120$ s. The new sticking-erosion model is able to capture the plateau effect seen in case No.3. The predicted ice tip

[‡]The plateau means the phenomenon that there is a maximum icing severity as a function of the melt ratio [15, 18, 38]. The severity will reduce by either increasing or reducing the melt ratio at the plateau. MR_c is the experimentally measured particle melt ratio at the middle of the inlet of the computational domain.

thicknesses, at $t = 120$ s, which are approximately 14, 27 and 4 mm, adequately match with the measurements, which are approximately 13, 30 and 2 mm respectively, when the mean MR at the centre of the inlet (referred to as MR_c) is increased from 4.7% (No.1) to 11% (No.3) and finally to 18.2% (No.4).

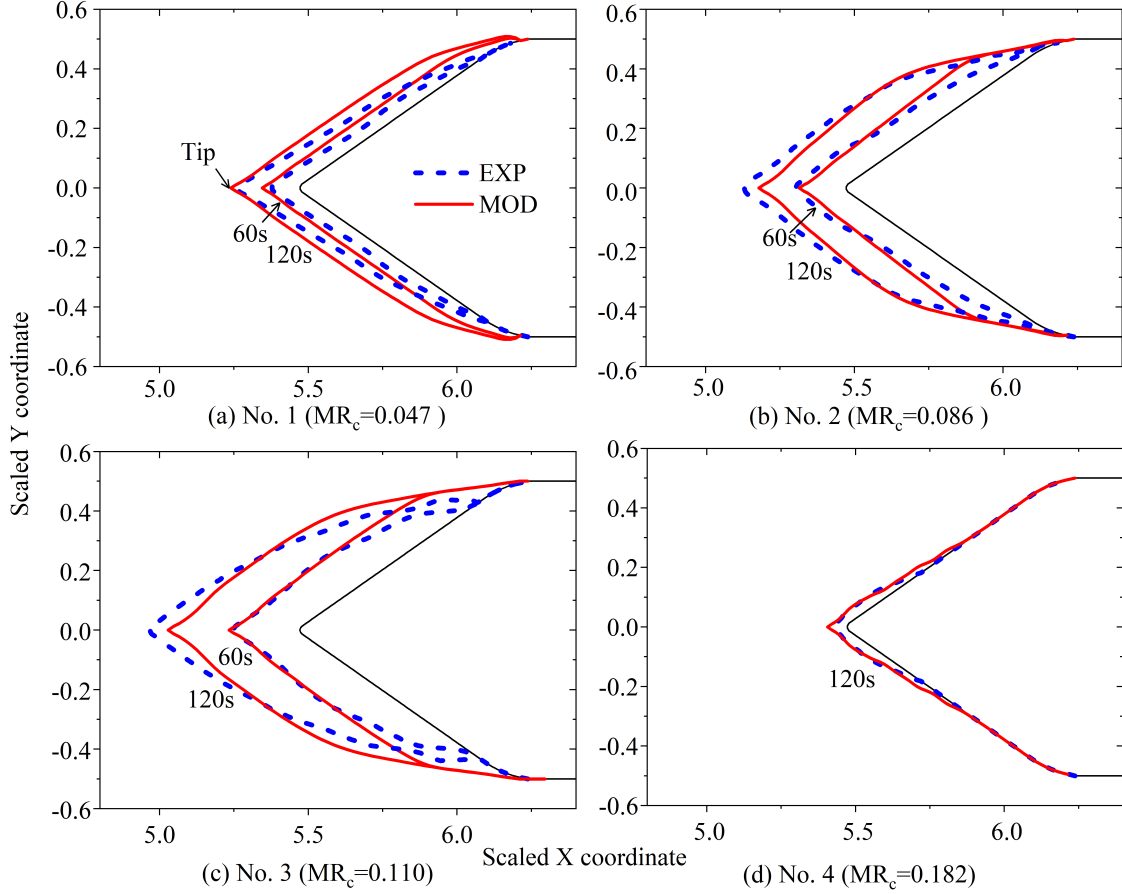


Fig. 11 The effect of MR on ice accretion at $Ma = 0.4$: (a) No.1 ($MR_c = 0.047$, $t = 60, 120$ s), (b) No.2 ($MR_c = 0.086$, $t = 60, 120$ s), (c) No.3 ($MR_c = 0.110$, $t = 60, 120$ s), and (d) No.4 ($MR_c = 0.182$, $t = 120$ s).

Figure 12 shows the effect of MR on the accretion profile for a lower $Ma = 0.25$ and $Dv50 = 29.5 \mu m$. The effect of MR on ice accretion at the lower Ma is similar to that at $Ma = 0.4$. Ice accretion rate shows a plateau effect at the MR_c of 11.9% (No.6). The predicted accretion profiles match reasonably with the measurements. The predicted ice tip thicknesses at t of 120 s, which are 8, 30 and 12 mm, are consistent with the measurements, which are approximately 12, 25 and 14 mm, at the MR_c of 6.1% (No.5), 11.9% (No.6) and 19.7% (No.7) [§]. Ma has two competing effects on ice accretion: (i) reducing Ma can decrease particle inertia, which will reduce particle impingement efficiency and ice accretion rate; (ii) reducing Ma can decrease particle erosion efficiency and increase ice accretion rate. For the cases with MR no higher than that at the plateau effect, the ice accretion rate at lower Ma is comparable to $Ma = 0.4$. However, for the case with MR above the plateau effect, the ice tip thickness (14 mm) at $Ma = 0.25$ is much higher

[§]More details of the ice tip thickness are given in Appendix VI.G

than that (2 mm) at $Ma = 0.4$. This indicates that the effect of Ma on increasing accretion rate via erosion-sticking is overwhelming the effect of Ma on reducing accretion rate via impingement.

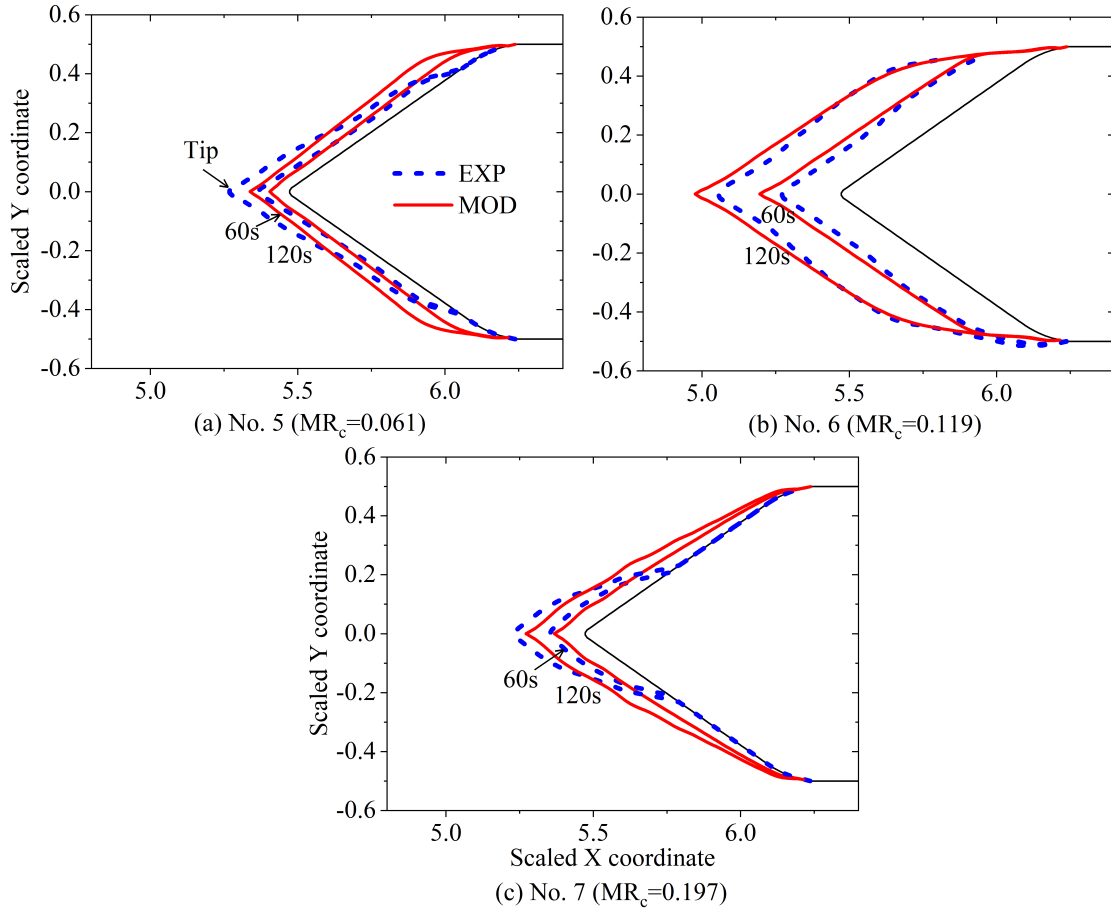


Fig. 12 The effect of MR on ice accretion at $Ma = 0.25$: (a) No.5 ($MR_c = 0.061$, $t = 60, 120$ s), (b) No.6 ($MR_c = 0.119$, $t = 60, 120$ s), and (c) No.7 ($MR_c = 0.197$, $t = 60, 120$ s).

Figure 13 shows a comparison of the predicted accretion profiles and the experimental measurements of two additional test articles: a cone with $\theta_h = 20^\circ$ and a stator vane. The predicted accretion profiles for the cone cases with $Ma = 0.25$ and 0.4 (No.10 and 11) match the experimental results reasonably. The predicted ice tip thickness at $t = 120$ s, ranging from 20 to 25 mm, are comparable to the measurements, ranging from 17 to 20 mm. For the stator vane cases at $Ma = 0.25$ and 0.4 (No.14 and 15), an extrusion of ice growth at the leading edge is observed in the predictions. This is consistent with the measured accretion profile. However, the predictions show some discrepancies, with an approximate 30-40% under-prediction of total accretion area compared with the measured profile. This discrepancy could be partially explained by the experimentally measured profile in the the stator vane cases being determined by the edge detection of two-dimensional accretion images taken looking across the span of the vane, and this may represent a local maximum in the accretion profile driven by 3D flow features which are not modelled in the fluid domain [39, 40]. For Fig. 13.d, the experimental accretion profile bends downwards, which is not captured by the prediction. This may

be because the leading edge accretion was relatively wet and hence a relatively low stiffness [41]. This can lead to the profile bending downwards under the aerodynamic load, which is not accounted for in the ICICLE.

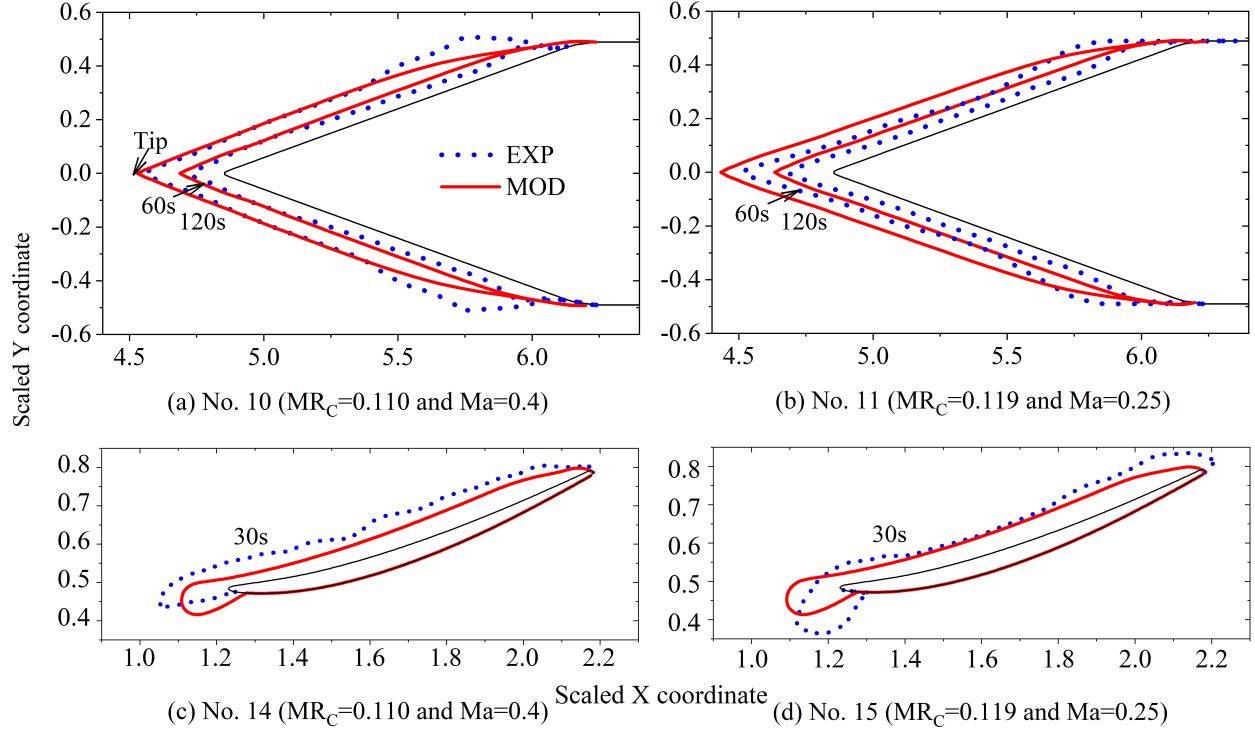


Fig. 13 Comparison of the predicted accretion profiles against the measurements of a cone with $\theta_h = 20^\circ$ and a stator vane: (a) No.10 ($MR_c = 0.110$ and $Ma = 0.4$, $t = 60, 120$ s), (b) No.11 ($MR_c = 0.119$ and $Ma = 0.25$, $t = 60, 120$ s), (c) No.14 ($MR_c = 0.110$, $Ma = 0.4$ and icing time = 30 s), and (d) No.15 ($MR_c = 0.119$, $Ma = 0.25$ and icing time = 30 s).

Figure 14 shows the effect of particle size on the accretion profile. For the cone cases ($\theta_h = 35^\circ$ and $Ma = 0.4$, see Fig. 14 (a)-(c)), the predicted accretion rate quickly drops with increasing particle size from PSD1 ($Dv_{10} = 14.7 \mu m$, $Dv_{50} = 29.5 \mu m$ and $Dv_{90} = 51.6 \mu m$) to PSD2 ($Dv_{10} = 22.3 \mu m$, $Dv_{50} = 41.6 \mu m$ and $Dv_{90} = 80.2 \mu m$). Likewise the predicted tip thickness decreases from approximately 27 mm to 2 mm. With a further increase in particle size to PSD3 ($Dv_{10} = 26.8 \mu m$, $Dv_{50} = 50.9 \mu m$ and $Dv_{90} = 102 \mu m$), no accretion is predicted. These results are in agreement with the general trend in the measured data, although the accretion has already dropped to zero when PSD2 was used. For the cone cases ($\theta_h = 20^\circ$ and $Ma = 0.25$, see Fig. 14 (d)-(f)), the predicted tip thickness decreases from 25.4 mm to 14.7 mm and then 4.9 mm, is comparable to the measurements, decreasing from approximately 20.1 mm to 11 mm and 0 mm, with increasing PSD from PSD1 to PSD2 and PSD4 ($Dv_{10} = 37.5 \mu m$, $Dv_{50} = 76.3 \mu m$ and $Dv_{90} = 139.3 \mu m$).

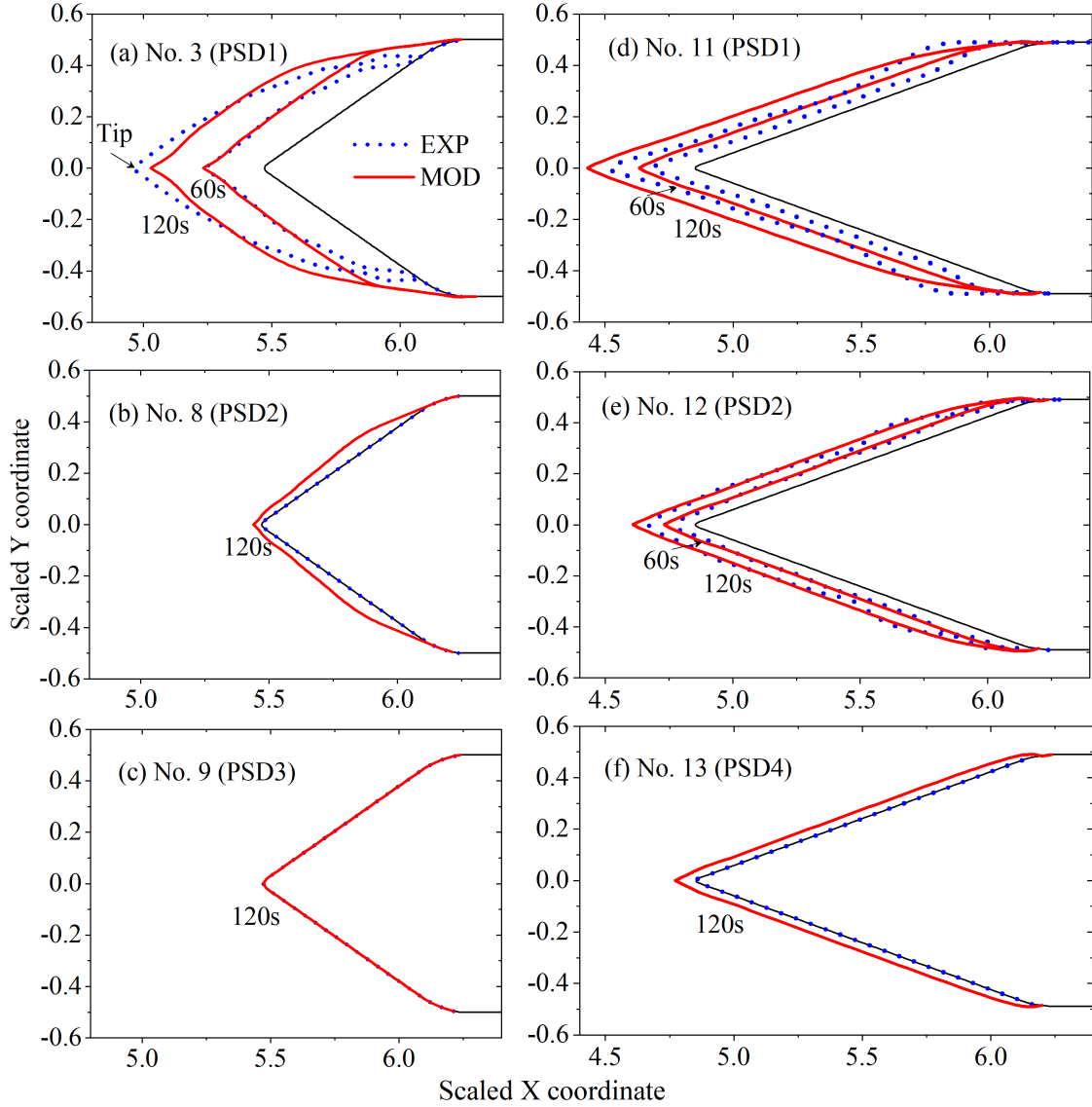


Fig. 14 The effect of PSD on ice accretion: (a) No.3 (PSD1, $Dv_{10} = 14.7 \mu m$, $Dv_{50} = 29.5 \mu m$ and $Dv_{90} = 51.6 \mu m$, $MR_c = 0.11$); (b) No.8 (PSD2, $Dv_{10} = 22.3 \mu m$, $Dv_{50} = 41.6 \mu m$ and $Dv_{90} = 80.2 \mu m$, $MR_c = 0.09$); (c) No.9 (PSD3, $Dv_{10} = 26.8 \mu m$, $Dv_{50} = 50.9 \mu m$ and $Dv_{90} = 102 \mu m$, $MR_c = 0.072$); (d) No.11 (PSD1, $MR_c = 0.119$); (e) No.12 (PSD2, $MR_c = 0.104$); (f) No.13 (PSD4, $Dv_{10} = 37.5 \mu m$, $Dv_{50} = 76.3 \mu m$ and $Dv_{90} = 139.3 \mu m$, $MR_c = 0.093$).

VI. Summary and Conclusions

A new sticking-erosion model using particle size distributions has been developed for modelling ice crystal icing at glaciated conditions. The model is generated from literature continued with new empirical relations developed to match data from a series of experiments generated in the NRC RATFac icing wind tunnel. The model is validated using a further series of independent tests conducted in the same facility.

In the model the particle sticking efficiency is taken to be a function of the melt ratios of both the particle and

accretion surface, using proven models from literature. To predict particle erosion efficiency, a dependence on particle velocity, particle size, impingement angle and accretion melt ratio are assumed. Using a trial functional form and a local minimisation process a set of constants for a new erosion model were obtained using individual particle impingement behaviour predicted from particle tracking and the experimental accretion data. The model is then first applied to additional operating conditions of the training geometry, and then further employed on alternative test geometries.

The main developments and findings from the work are:

- 1) For the first time, the size selective accretion behaviour of ice crystals is presented in the range $D=5 - 80 \mu m$. For the baseline case, small-medium particles ($\sim 15 \mu m$) are easier to accrete than either the smallest or largest particles. This results from the dependence of particle impingement, sticking and erosion behaviours on particle size. Particle accretion efficiency reduces with the increasing particle size (in the medium-large range). The efficiency becomes negative value for the largest particles. This indicates that large particles are mainly contribute to ice removal rather than accretion. It also highlights the need to model a full particle size distribution rather than determining a representative mean value.
- 2) The predicted accretion profiles are consistent with experimental data over a range of MR, Ma, test article geometry and PSD. The mean difference of the ice tip thickness between predictions and experiments for all the 15 cases modelled is 2.8 mm and the maximum difference is 5.3mm, compared to the mean ice tip thickness of 12.0 mm and the maximum thickness of 30.4 mm.
- 3) The predicted plateau effect with MR matches experiments adequately at $Ma = 0.25$ and 0.4 . However, it is still noticeable that the new model cannot accurately predict some subtle features such as the lack of stable accretion in the rear region of cone front surface, where shedding events dominate the net accretion behaviour.
- 4) The accretion profiles of the alternative test geometries are captured by the predictions, especially for the two cone cases with $\theta_h = 20^\circ$. For the stator vane cases, the predictions show 30% to 40% less accretion than the experimental data. This is due to that the experimental data of the stator vane cases may represent a local maximum accretion driven by 3D flow features which are not modelled in the fluid domain.
- 5) The predicted effect of PSD on ice accretion agrees with the experimental data although the experimental accretion rate drops to zero at a relatively smaller PSD. This indicates that the erosion rate may be slightly underestimated at larger PSD. This discrepancy leads to the tip ice thickness over-predicted by 2-5mm.

Appendix

A. Operation conditions

Table 3 Operating conditions of the ICI experiments considered: the symbol next to test number, *, represents the test case used for training; No. 14 and 15 are stator vane cases.

No.	$TWC, g/m^3$	$T_0, ^\circ C$	P_0, kPa	Ma	RH	$Dv_{10}, Dv_{50}, Dv_{90}, MVD, \mu m$	$\theta_h, ^\circ$
<u>1*</u>	8	10	34.5	0.4	0.3	14.7, 29.5, 51.6, 30.8	35
<u>2*</u>	8	10	34.5	0.4	0.4	14.7, 29.5, 51.6, 30.8	35
<u>3*</u>	8	10	34.5	0.4	0.45	14.7, 29.5, 51.6, 30.8	35
<u>4*</u>	8	10	34.5	0.4	0.65	14.7, 29.5, 51.6, 30.8	35
5	8	10	34.5	0.25	0.3	14.7, 29.5, 51.6, 30.8	35
<u>6*</u>	8	10	34.5	0.25	0.45	14.7, 29.5, 51.6, 30.8	35
7	8	10	34.5	0.25	0.65	14.7, 29.5, 51.6, 30.8	35
<u>8*</u>	8	10	34.5	0.4	0.45	22.3, 41.6, 80.2, 46.8	35
9	8	10	34.5	0.4	0.45	26.8, 50.9, 102.0, 57.9	35
<u>10*</u>	8	10	34.5	0.4	0.45	14.7, 29.5, 51.6, 30.8	20
11	8	10	34.5	0.25	0.45	14.7, 29.5, 51.6, 30.8	20
12	8	10	34.5	0.25	0.45	22.3, 41.6, 80.2, 46.8	20
13	8	10	34.5	0.25	0.45	37.5, 76.3, 139.3, 81.3	20
14	8	10	34.5	0.4	0.45	14.7, 29.5, 51.6, 30.8	NA
15	8	10	34.5	0.25	0.45	14.7, 29.5, 51.6, 30.8	NA

B. Comparison of the baseline PSD and the Langmuir distributions.

Figure 15 shows the comparison of the measured baseline PSD, the Rosin-Rammler based PSD transferred from the measurement, and the Langmuir distributions. The Langmuir distributions, which are used in supercooled water icing analysis, are pre-defined PSDs [42]. Therefore, it is expected that the Langmuir distributions may be not able to fully represent the PSD of ice crystal particles. As shown in Fig.15, the curves of the Langmuir B and C distributions are steeper than the Rosin-Rammler curve. This indicates that the Langmuir B and C distributions under-predict the concentration fraction of relatively smaller and larger PSD and over-predict the concentration fraction of PSD in the middle range of the PSD. The Langmuir D shows a lower concentration fraction of relatively smaller PSD (the ratio of particle diameter to $Dv_{50} < 1$) as the Langmuir D curve locates on the right hand side of the Rosin-Rammler curve. The Langmuir E shows a higher concentration fraction of relatively larger PSD (the ratio of particle diameter to $Dv_{50} > 1.7$) as the Langmuir E curve locates on the right hand side of the Rosin-Rammler curve.

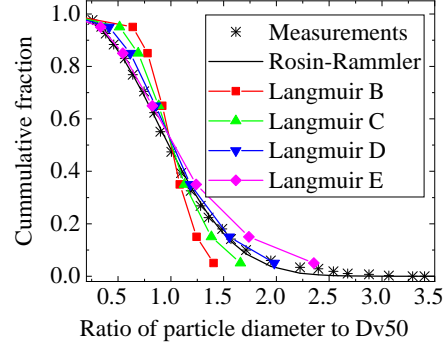


Fig. 15 Comparison of the baseline PSD and the Langmuir distributions.

C. The term ③ in the erosion equation (Equation (4))

The main difference in the operation conditions among Cases No. 1-4 is humidity. This indicates that the major difference is particle melt ratio for Cases No. 1-4. Therefore, the four cases are used for the optimization of the term ③. Figure 16 shows the comparison of the term ③ in the erosion equation between the prediction and experimental derived value as a function of melt ratio. It can be seen that the experimentally derived term ③ initially increases with the mean particle impingement melt ratio (MR_m) increased from approximately 0.02 to 0.1 and then the erosion efficiency, ranging from 0.005 to 0.01, fluctuates at the melt ratio between 0.1 and 0.2. When the melt ratio further increases to approximately 0.33, the value of the term increases to approximately 0.016. The predicted values using the optimized model constants agree with the experimentally derived data.

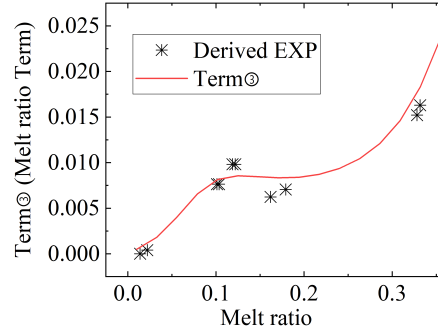


Fig. 16 Comparison of the term ③ in the erosion equation between the prediction and experimental derived value.

D. The effect of the 2D assumption on the ice accretion

In order to clarify the effect of the 2D axisymmetric assumption on the ice accretion, particle tracking is carried out for the 2D axisymmetric flowfield and 3D flowfield (only the flowfield of the middle cutplane is used for ICICLE). Figure 17 shows the particle impingement behaviours (melt ratio, impingement velocity, impingement angle, and mean impingement particle size) for the 2D and 3D flowfields. It can be observed that particle impingement behaviours

using the 2D flowfield are similar to those using the 3D flowfield. This is because the upstream flowfield (velocity and temperature) are close for the two cases as shown in the Fig.18. The main difference in the flowfield is at the horizontal and downstream regions of the cone, which will not affect the ice accretion at the cone nose.

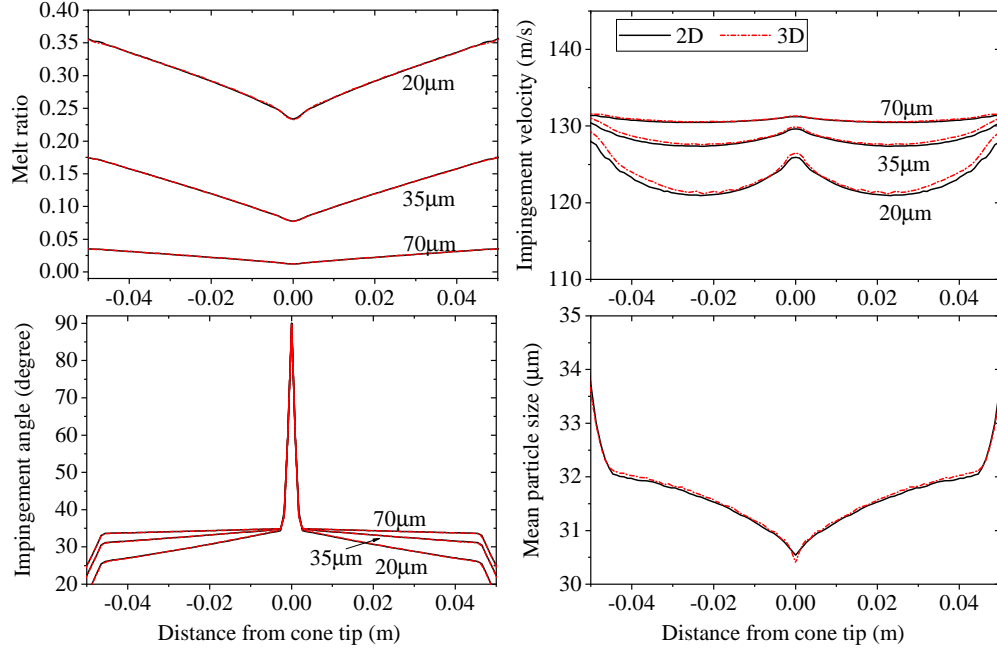


Fig. 17 Comparison of the particle impingement behaviours (melt ratio, impingement velocity, impingement angle, and mean impingement particle size) between the 2D and 3D flowfields.

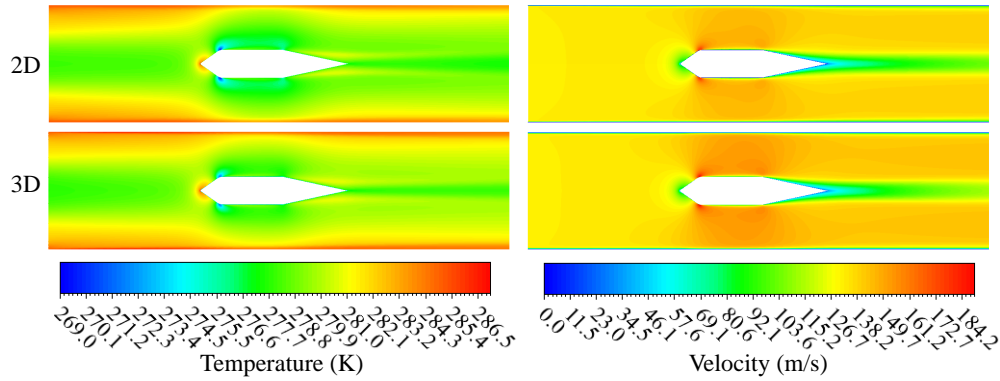


Fig. 18 Comparison of the 2D and 3D flowfields.

E. Melt ratio map at inlet

Figure 19 shows the particle melt ratio at the inlet versus particle size. All the sub-figures show similar features: (i) small particles have higher melt ratio; (ii) melt ratio is higher at the center region. The differences of melt ratios among these figures are caused by the difference in the operation conditions (relative humidity, Mach number and particle size distribution).

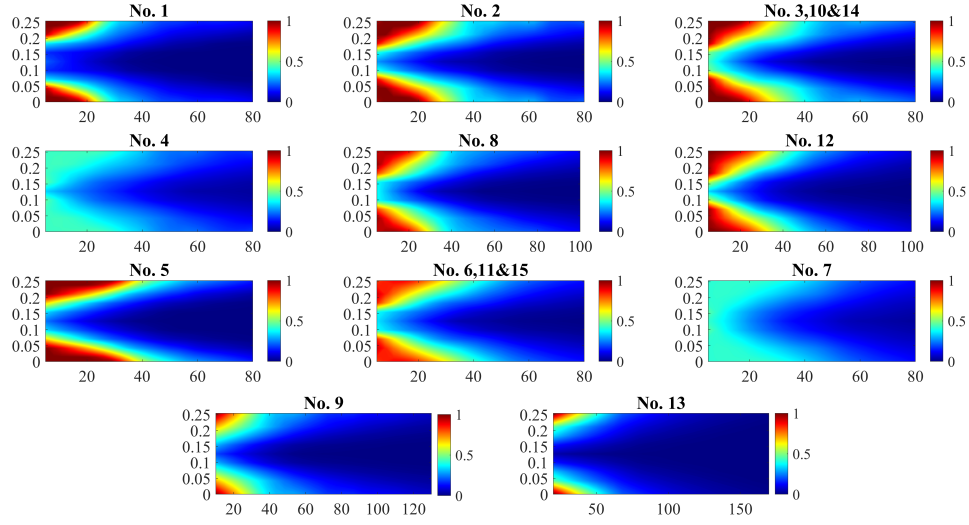


Fig. 19 The particle melt ratio contour at the inlet of the computational domain as a function of particle size for all cases.

F. Shedding on the rear region of the cone nose

Figure 20 is an example of ice shedding on the rear region of the cone nose for the baseline case. It is observed that the shedding of ice appears in the region highlighted by the green rectangular box. This leads to no ice accretion on the region. This phenomenon is not captured by the prediction as the ice shedding is not considered in the current model.

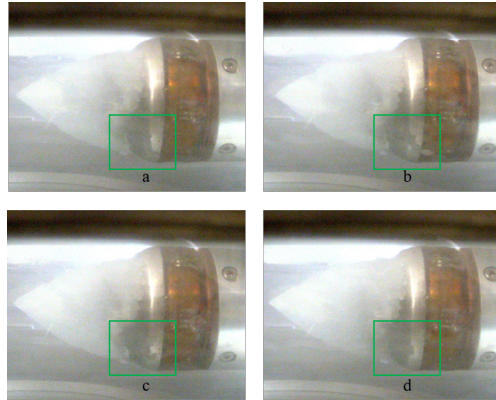


Fig. 20 An example of shedding on the rear region of the cone nose.

G. Ice tip thickness

Table 4 shows the ice tip thickness between the predictions and the experimental data. For all the 15 cases (120s for cone cases and 30s for stator cases), the mean experimental tip thickness is approximately 12.0 mm and the maximum tip thickness is 30.4 mm. The mean difference of the ice tip thickness between the predictions and the experimental data is approximately 2.8 mm and the maximum difference is 5.3 mm.

Table 4 Comparison of the ice tip thickness (mm) between the predictions and the experimental data.

	No.1		No.2		No.3		No.4	No.5		No.6		No.7	
Data	60s	120s	60s	120s	60s	120s	120s	60s	120s	60s	120s	60s	120s
EXP	5.7	12.5	10.1	20.5	13.4	30.4	2.4	6.3	12.3	12.1	25.0	7.2	14.2
MOD	7.7	14.0	9.5	17.6	14.4	26.7	4.0	4.1	8.1	16.7	29.9	6.4	11.2
	No.8	No.9	No.10		No.11		No.12		No.13	No.14	No.15		
Data	120s	120s	60s	120s	60s	120s	60s	120s	120s	30s	30s		
EXP	0	0	7.4	17.3	9.9	20.1	4.6	11.0	0	7.9	6.1		
MOD	2	0	10.0	19.6	13.3	25.4	7.3	14.7	4.9	5.4	6.0		

Acknowledgments

The authors would like to acknowledge Rolls-Royce plc and the Aerospace Technology Institute (ATI) for the funding provided within the DE-ICER programme (Grant number: 113155) which supported this research.

References

- [1] Mason, J., Strapp, W., and Chow, P., “The ice particle threat to engines in flight,” *44th AIAA Aerospace Sciences Meeting and Exhibit*, AIAA Paper 2006-206, 2006. <https://doi.org/10.2514/6.2006-206>.
- [2] Bravin, M., Strapp, J. W., and Mason, J., “An Investigation into Location and Convective Lifecycle Trends in an Ice Crystal Icing Engine Event Database,” *SAE 2015 International Conference on Icing of Aircraft, Engines, and Structures*, SAE Paper 2015-01-2130, 2015. <https://doi.org/10.4271/2015-01-2130>.
- [3] Haggerty, J., Defer, E., Laat, A. D., Bedka, K., Moisselin, J.-M., Potts, R., Delanoë, J., Parol, F., Grandin, A., and Divito, S., “Detecting Clouds Associated with Jet Engine Ice Crystal Icing,” *Bulletin of the American Meteorological Society*, Vol. 100, No. 1, 2019, pp. 31 – 40. <https://doi.org/10.1175/BAMS-D-17-0252.1>.
- [4] Wright, W., Jorgenson, P., and Veres, J., “Mixed phase modeling in GlennICE with application to engine icing,” *AIAA Atmospheric and Space Environments Conference*, AIAA Paper 2010-7674, 2010. <https://doi.org/10.2514/6.2010-7674>.
- [5] Villedieu, P., Trontin, P., and Chauvin, R., “Glaciated and mixed phase ice accretion modeling using ONERA 2D icing suite,” *6th AIAA Atmospheric and Space Environments Conference*, AIAA Paper 2014-2199, 2014. <https://doi.org/10.2514/6.2014-2199>.
- [6] Radenac, E., Bayeux, C., and Villedieu, P., “Use of a Two-Dimensional Finite Volume Integral Boundary-Layer Method for Ice-Accretion Calculations,” *AIAA Journal*, Vol. 58, No. 4, 2020, pp. 1592–1606. <https://doi.org/10.2514/1.J058701>.
- [7] Habashi, W., and Nilamdeen, S., “Multiphase approach toward simulating ice crystal ingestion in jet engines,” *Journal of Propulsion and Power*, Vol. 27, No. 5, 2011, pp. 959–969. <https://doi.org/10.2514/1.B34059>.
- [8] Norde, E., van der Weide, E. T. A., and Hoeijmakers, H. W. M., “Eulerian Method for Ice Crystal Icing,” *AIAA journal*, Vol. 56, No. 1, 2017, pp. 222–234. <https://doi.org/10.2514/1.J056184>.

- [9] Norde, E., Senoner, J.-M., van der Weide, E. T. A., Trontin, P., Hoeijmakers, H. W. M., and Villedieu, P., "Eulerian and Lagrangian Ice-Crystal Trajectory Simulations in a Generic Turbofan Compressor," *Journal of Propulsion and Power*, Vol. 35, No. 1, 2019, pp. 26–40. <https://doi.org/10.2514/1.B36916>.
- [10] Bucknell, A., McGilvray, M., Gillespie, D., Yang, X., Jones, G., and Collier, B., "ICICLE: A Model for Glaciated & Mixed Phase Icing for Application to Aircraft Engines," *International Conference on Icing of Aircraft, Engines, and Structures*, SAE Paper 2019-01-1969, 2019. <https://doi.org/10.4271/2019-01-1969>.
- [11] Yang, X., McGilvray, M., and Gillespie, D. R., "Modelling the particle trajectory and melting behaviour of non-spherical ice crystal particles," *International Journal of Multiphase Flow*, Vol. 148, 2022, p. 103949. <https://doi.org/10.1016/j.ijmultiphaseflow.2021.103949>.
- [12] Lozowski, E. P., Stallabrass, J. R., and Hearty, P. F., "The Icing of an Unheated, Nonrotating Cylinder. Part I: A Simulation Model," *Journal of Climate and Applied Meteorology*, Vol. 22, No. 12, 1983, pp. 2053–2062. [https://doi.org/10.1175/1520-0450\(1983\)022<2053:TIOAUN>2.0.CO;2](https://doi.org/10.1175/1520-0450(1983)022<2053:TIOAUN>2.0.CO;2).
- [13] Al-Khali, K., "Assessment of effects of mixed-phase icing conditions on thermal ice protection systems," *Department of Transportation, Federal Aviation Administration*, DOT/FAA/AR-03/48, 2003.
- [14] Ayan, E., and Özgen, S., "In-flight ice accretion simulation in mixed-phase conditions," *The Aeronautical Journal*, Vol. 122, No. 1249, 2018, pp. 409–441. <https://doi.org/10.1017/aer.2017.127>.
- [15] Baumert, A., Bansmer, S., Trontin, P., and Villedieu, P., "Experimental and numerical investigations on aircraft icing at mixed phase conditions," *International Journal of Heat and Mass Transfer*, Vol. 123, 2018, pp. 957–978. <https://doi.org/10.1016/j.ijheatmasstransfer.2018.02.008>.
- [16] Nilamdeen, S., Rao, V. S., Switchenko, D., Selvanayagam, J., Ozcer, I., and Baruzzi, G. S., "Numerical Simulation of Ice Crystal Accretion Inside an Engine Core Stator," *International Conference on Icing of Aircraft, Engines, and Structures*, SAE paper 2019-01-2017, 2019. <https://doi.org/10.4271/2019-01-2017>.
- [17] Currie, T. C., Fuleki, D., and Mahallati, A., "Experimental studies of mixed-phase sticking efficiency for ice crystal accretion in jet engines," *6th AIAA Atmospheric and Space Environments Conference*, AIAA paper 2014-3049, 2014. <https://doi.org/10.2514/6.2014-3049>.
- [18] Bucknell, A., McGilvray, M., Gillespie, D. R. H., Jones, G., Reed, A., and Collier, B., "Experimental Studies of Ice Crystal Accretion on Axisymmetric Bodies at Aeroengine Conditions," *Journal of Propulsion and Power*, Vol. 36, No. 6, 2020, pp. 836–850. <https://doi.org/10.2514/1.B37635>.
- [19] Currie, T. C., "Event-Driven Simulation of Particle-Particle and Particle-Surface Collisions in Ice Crystal Icing," *International Conference on Icing of Aircraft, Engines, and Structures*, SAE paper 2019-01-2014, 2019. <https://doi.org/10.4271/2019-01-2014>.

- [20] Trontin, P., and Villedieu, P., “A comprehensive accretion model for glaciated icing conditions,” *International Journal of Multiphase Flow*, Vol. 108, 2018, pp. 105–123. <https://doi.org/10.1016/j.ijmultiphaseflow.2018.06.023>.
- [21] Charton, V., Senoner, J.-M., Trontin, P., and Villedieu, P., “Semi-empirical Erosion Model with Particle Size and Liquid Water Content Effects for Ice Crystal Icing Simulations,” *AIAA AVIATION 2020 FORUM*, AIAA paper 2020-2827, 2020. <https://doi.org/10.2514/6.2020-2827>.
- [22] Knezevici, D., Fuleki, D., Currie, T., and MacLeod, J., “Particle size effects on ice crystal accretion,” *4th AIAA Atmospheric and Space Environments Conference*, AIAA Paper 2012-3039, Sep. 2012, p. 3039. <https://doi.org/10.2514/6.2012-3039>.
- [23] Walsh, P. M., Sayre, A. N., Loehden, D. O., Monroe, L. S., Beér, J. M., and Sarofim, A. F., “Deposition of bituminous coal ash on an isolated heat exchanger tube: Effects of coal properties on deposit growth,” *Progress in Energy and Combustion Science*, Vol. 16, No. 4, 1990, pp. 327–345. [https://doi.org/10.1016/0360-1285\(90\)90042-2](https://doi.org/10.1016/0360-1285(90)90042-2).
- [24] Yang, X., Ingham, D., Ma, L., Zhou, H., and Pourkashanian, M., “Understanding the ash deposition formation in Zhundong lignite combustion through dynamic CFD modelling analysis,” *Fuel*, Vol. 194, 2017, pp. 533 – 543. <https://doi.org/10.1016/j.fuel.2017.01.026>.
- [25] Currie, T., and Fuleki, D., “Development and Application of an Impedance-Based Instrument for Measuring the Liquid Fraction and Thickness of Ice Crystal Accretions,” *SAE 2015 International Conference on Icing of Aircraft, Engines, and Structures*, SAE paper 2015-01-2134, 2015. <https://doi.org/10.4271/2015-01-2134>.
- [26] Finnie, I., and McFadden, D., “On the velocity dependence of the erosion of ductile metals by solid particles at low angles of incidence,” *Wear*, Vol. 48, No. 1, 1978, pp. 181 – 190. [https://doi.org/10.1016/0043-1648\(78\)90147-3](https://doi.org/10.1016/0043-1648(78)90147-3).
- [27] Bitter, J., “A study of erosion phenomena part I,” *Wear*, Vol. 6, No. 1, 1963, pp. 5 – 21. [https://doi.org/10.1016/0043-1648\(63\)90003-6](https://doi.org/10.1016/0043-1648(63)90003-6).
- [28] Bitter, J., “A study of erosion phenomena: Part II,” *Wear*, Vol. 6, No. 3, 1963, pp. 169 – 190. [https://doi.org/10.1016/0043-1648\(63\)90073-5](https://doi.org/10.1016/0043-1648(63)90073-5).
- [29] Kott, B., Struk, P. M., and Bartkus, T. P., “A Study of Ice-Crystal Icing Erosion Using the NASA Icing Research Tunnel and Propulsion Systems Laboratory,” *AIAA AVIATION 2020 FORUM*, AIAA paper 2020-2842, 2020, p. 2842. <https://doi.org/10.2514/6.2020-2842>.
- [30] Neilson, J., and Gilchrist, A., “Erosion by a stream of solid particles,” *Wear*, Vol. 11, No. 2, 1968, pp. 111–122. [https://doi.org/10.1016/0043-1648\(68\)90591-7](https://doi.org/10.1016/0043-1648(68)90591-7).
- [31] Nonato, L. G., Mangiavacchi, N., Sousa, F. S., Castelo, A., and Cuminato, J. A., “A mass-conserving smooth method,” *Mecánica Computacional*, Vol. XXIII, No. 18, 2004, pp. 1897–1910.
- [32] Yang, X., McGilvray, M., and Gillespie, D., “Numerical Modeling and Parametric Study of the Melting Behavior of Ice Crystal Particles,” *AIAA Journal*, Vol. 59, No. 11, 2021, pp. 4660–4668. <https://doi.org/10.2514/1.J060351>.

- [33] Tsuji, Y., Oshima, T., and Morikawa, Y., “Numerical Simulation of Pneumatic Conveying in a Horizontal Pipe,” *KONA Powder and Particle Journal*, Vol. 3, 1985, pp. 38–51. <https://doi.org/10.14356/kona.1985009>.
- [34] Bucknell, A., McGilvray, M., Gillespie, D. R., Jones, G., and Collier, B., “A thermodynamic model for ice crystal accretion in aircraft engines: EMM-C,” *International Journal of Heat and Mass Transfer*, Vol. 174, 2021, p. 121270. <https://doi.org/10.1016/j.ijheatmasstransfer.2021.121270>.
- [35] Knezevici, D. C., Fuleki, D., and MacLeod, J., “Development and Commissioning of a Linear Compressor Cascade Rig for Ice Crystal Research,” *SAE 2011 International Conference on Icing of Aircraft, Engines, and Structures*, SAE Paper 2011-38-0079, 2011. <https://doi.org/10.4271/2011-38-0079>.
- [36] Struk, P., Currie, T., Wright, W. B., Knezevici, D. C., Fuleki, D., Broeren, A., Vargas, M., and Tsao, J.-C., “Fundamental Ice Crystal Accretion Physics Studies,” *SAE 2011 International Conference on Aircraft and Engine Icing and Ground Deicing*, SAE paper 2011-38-0018, 2011. <https://doi.org/10.4271/2011-38-0018>.
- [37] Trontin, P., Blanchard, G., Kontogiannis, A., and Villedieu, P., “Description and assessment of the new ONERA 2D icing suite IGLOO2D,” *9th AIAA Atmospheric and Space Environments Conference*, AIAA Paper 2017-3417, 2017. <https://doi.org/10.2514/6.2017-3417>.
- [38] Currie, T., Struk, P., Tsao, J.-C., Fuleki, D., and Knezevici, D., “Fundamental study of mixed-phase icing with application to ice crystal accretion in aircraft jet engines,” *4th AIAA Atmospheric and Space Environments Conference*, AIAA Paper 2012-3035, Jun. 2012, p. 3035. <https://doi.org/10.2514/6.2012-3035>.
- [39] Parker, L., McGilvray, M., and Gillespie, D., “Modelling and Simulation of Mixed Phase Ice Crystal Icing in Three-Dimensions,” *International Conference on Icing of Aircraft, Engines, and Structures*, SAE Paper 2023-01-1475, 2023.
- [40] Connolly, J., McGilvray, M., and Gillespie, D. R., “Optical measurement of ice crystal icing on a NACA 0018 airfoil,” *AIAA AVIATION 2022 Forum*, AIAA Paper 2022-3699, 2022. <https://doi.org/10.2514/6.2022-3699>.
- [41] Connolly, J. P., McGilvray, M., Gillespie, D., Bucknell, A., Parker, L., Jones, G., and Collier, B., “Two-Way Flow Coupling in Ice Crystal Icing Simulation,” *International Conference on Icing of Aircraft, Engines, and Structures*, SAE Paper 2019-01-1966, 2019. <https://doi.org/10.4271/2019-01-1966>.
- [42] Langmuir, I., and Katherine B., B., “A mathematical investigation of water droplet trajectories,” U.S. Army Air Force Technical Report No. 5418, 1946.